

Rotating quantum turbulence in the unitary Fermi gas

Konrad Kobuszewski,¹ Khalid Hossain,² Michael McNeil Forbes,^{2,3}
Piotr Magierski,^{1,3} Kazuyuki Sekizawa,^{4,5} and Gabriel Wlazłowski^{1,3,*}

¹*Faculty of Physics, Warsaw University of Technology, Ulica Koszykowa 75, 00-662 Warsaw, Poland[†]*

²*Department of Physics and Astronomy, Washington State University, Pullman, WA 99164, USA*

³*Department of Physics, University of Washington, Seattle, Washington 98195-1560, USA[‡]*

⁴*Center for Transdisciplinary Research, Institute for Research Promotion, Niigata University, Niigata 950-2181, Japan*

⁵*Division of Nuclear Physics, Center for Computational Sciences, University of Tsukuba, Ibaraki 305-8577, Japan*

Quantized vortices carry the angular momentum in rotating superfluids, and are key to the phenomenon of quantum turbulence. Advances in ultra-cold atom technology enable quantum turbulence to be studied in regimes with both experimental and theoretical control, unlike the original contexts of superfluid helium experiments. While much work has been performed with bosonic systems, detailed studies of fermionic quantum turbulence are nascent, despite wide applicability to other contexts such as rotating neutron stars. In this paper, we present the first large-scale study of quantum turbulence in rotating fermionic superfluids using an accurate orbital based time-dependent density functional theory (DFT) called the superfluid local density approximation (SLDA). We identify two different modes of turbulent decay in the dynamical equilibration of a rotating fermionic superfluid, and contrast these results with a computationally simpler orbital-free DFT, which we find can qualitatively reproduce these decay mechanisms if dissipation is explicitly included. These results demonstrate that one-body dissipation mechanisms intrinsic to fermionic superfluids play a key role differentiating fermionic from bosonic turbulence, but also suggest that simpler orbital-free theories may be corrected so that these more efficient techniques can be used to model extended physical systems such as neutron superfluids in neutron stars.

Introduction—Quantized vortices are a direct manifestation of superfluidity. In rotating systems, they relax into a regular structure known as an Abrikosov lattice [1]. This lattice can be destroyed by external perturbations, leading to the appearance of quantum turbulence—complex non-equilibrium flow with tangled vortices. Within the tangle, vortices collide and reconnect, transferring energy between length scales, bringing the system back towards equilibrium, and giving rise to an effective dissipation at large scales, despite the superfluid nature of the system. These turbulent processes have been observed in rotating systems with superfluid ³He [2–5] and ⁴He experiments [6, 7]. Here, we study this phenomenon in an ultracold atomic gas of strongly interacting fermions—the unitary Fermi gas (UFG). In the UFG, the ratio of the pairing gap to the Fermi energy $\Delta/\varepsilon_F \approx 0.5$ attains the largest known value, and the corresponding coherence length $\xi \approx 1/k_F$ becomes very short, on the order of the average inter-particle separation. The UFG can thus maintain a high density of vortex lines in a robust superfluid with a high Landau critical velocity of the order of the Fermi velocity [8]. These features, in combination with experimental access, make the UFG an ideal platform to study quantum turbulence in a new regime that cannot be accessed in superfluid helium or in cold-atom Bose-Einstein condensates (BECs) [9].

Direct numerical studies of turbulent dynamics in Fermi systems are very challenging. The high vortex-line density means that one cannot separate length scales associated with mean inter-vortex distance from the size of the vortex core, precluding the use of mesoscopic vortex filament models (VFMs) [10]. Instead, a microscopic

approach is required. For weakly interacting bosons at $T = 0$, a time-dependent nonlinear Schrödinger equation is justified: the Gross-Pitaevskii equation (GPE) (see e.g. [11]). This is a form of orbital-free density functional theory (DFT) and generalizations of the GPE have been used to model fermionic superfluids [12–18]. Fermions differ fundamentally from bosons because of effects of the Pauli exclusion principle. While in general, these can be incorporated into an orbital-free approach, how to do this is an unsolved problem, and form of the generalized GPE lacks this sophistication. Nevertheless, the orbital-free approach to condensate dynamics is computationally simple, and captures many qualitative effects [16].

Its form is described in the supplement [19] and we use it as a baseline for comparison. When we refer to the GPE in this paper, we mean this generalized orbital-free approach.

To account for exclusion effects, one must currently use an orbital-based DFT such as the Bogoliubov-de Gennes (BdG) or Hartree-Fock Bogoliubov (HFB). We use a DFT called the time-dependent asymmetric superfluid local density approximation (TDASLDA) [22, 23] that has been carefully validated against experiments and quantum Monte-Carlo calculations at the few-percent level for static properties [22–25]. Quantitative validation at the same level for dynamics is ongoing [26–28], and a motivation for this paper. The TDASLDA introduces significant differences from the GPE, correctly accounting for the filling of fermionic vortex cores with a “normal” component [29–31], even at $T = 0$. The structure of the vortex core is also sensitive to spin-imbalance [32, 33], which affects its size and generates reversed flow [34].

By changing spin imbalance of the system, one can thus control amount of the normal component, and modify intensity of dissipative processes. This work advances our understanding of fermionic superfluidity in the turbulent regime, which has important consequences for superfluids in cold-atom experiments, and neutron stars.

In particular, we investigate the mechanism of turbulent decay and compare with the simpler orbital-free approach, GPE, thus providing an insight into the role of fermionic degrees of freedom outside the condensate in the decay process.

Numerical simulations — We numerically simulate the UFG close to the zero temperature limit with two fully microscopic approaches: an orbital-based TDASLDA with explicit fermionic degrees of freedom, and an orbital-free GPE which models the condensate with a single wavefunction. The TDASLDA allows us to also study spin-imbalanced systems, with unequal numbers of spin up (N_\uparrow) and spin down (N_\downarrow) atoms. This approach has been applied to a variety of systems, including ultra-cold atomic gases [26–28, 35], atomic nuclei [36–38] and neutron star crusts [39]. In particular, we demonstrate [28] that the TDASLDA correctly captures the dynamics and evolution of topological excitations, including quantized vortices, by comparing with experiments. The exact form of the TDASLDA is described in [22]: this has the same structure as the commonly used BdG equations, but includes carefully tuned Hartree terms.

The comparison with a GPE simulation of the form described in [16, 19] has been performed for the dimer/Cooper-pair wavefunction $\Psi(\mathbf{r}, t)$ with mass $m_D = 2m$ and dimer number-density $n_D = n_F/2 = |\Psi|^2$, and by replacing the GPE energy-density $gn_D^2/2$ by the energy-density of the UFG $\xi\mathcal{E}_{FG}(n_F)$. The GPE lacks any mechanism for dissipating hydrodynamic energy into internal degrees of freedom.

To account for this, we introduce a small amount of dissipation by altering the time evolution: $i\hbar\frac{\partial\Psi}{\partial t} \rightarrow i\hbar e^{i\eta}\frac{\partial\Psi}{\partial t}$, which involve phenomenological parameter η .

To ensure conservation of particle number and approximate conservation of angular momentum, we include a dynamically adjusted chemical potential $\mu[\Psi]$, and simulate in a co-rotating frame with angular velocity Ω matching the initial state.

We evolve both TDASLDA and GPE equations numerically on 3D spatial grids of size $50 \times 50 \times 100$ with lattice spacing $dx = k_F^{-1} \approx 0.78\xi$, where $\xi = k_F/\pi\Delta$ is the BCS coherence length (here and below we use natural units where $m = \hbar = 1$). The gas is confined with a flat-bottomed trapping potential $V_{\text{ext}}(x^2 + y^2)$ to a tube of a radius $18dx$ with periodic boundary conditions along z . The number of particles is adjusted so that the Fermi momentum of majority spin component $k_F = \sqrt{2\varepsilon_F} = (6\pi^2 n_\uparrow)^{1/3} \approx 1$ in the initial state, where n_\uparrow is local density of spin-up particles at the center of the trap. (See [19] for precise details.)

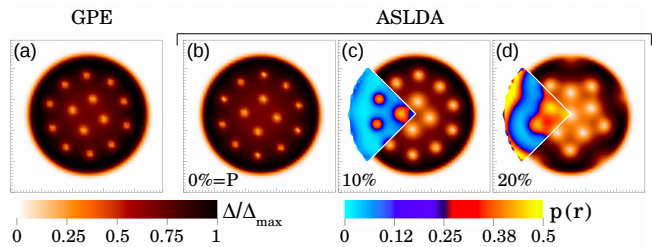


FIG. 1. Cross sections of the initial states used for generation of quantum turbulence obtained within two complementary approaches: GPE (a) and ASLDA (b)-(d). Panels show normalized order parameter $|\Delta(\mathbf{r})|$ with respect to its maximal value, respectively for spin symmetric case $P = 0\%$ (a)-(b), and spin polarized cases $P = 10\%$ (c) and 20% (d). On panels (c) and (d) in quarter on left the local polarization $p(\mathbf{r})$ is displayed.

Under these conditions, the trap comprises $N_\uparrow + N_\downarrow \approx 3500$ atoms.

To generate the quantum turbulence, we start from a self-consistent (stationary) configuration of 14 vortices in a lattice that minimizes the energy in the frame rotating with angular velocity $\Omega = -0.05\varepsilon_F$.

In Fig. 1 we present the solutions for systems with global polarization equal to $P = 0\%$, 10% and 20% , where $P = (N_\uparrow - N_\downarrow)/(N_\uparrow + N_\downarrow)$. For relatively small spin imbalances, the excess spin component accumulates in the vortex cores, changing their size. The maximum local spin polarization $p(\mathbf{r}) = \frac{n_\uparrow(\mathbf{r}) - n_\downarrow(\mathbf{r})}{n_\uparrow(\mathbf{r}) + n_\downarrow(\mathbf{r})}$ is 40%–45% in the $P = 10\%$ case. Further increase of the imbalance modifies the lattice structure, as seen already in the case of $P = 20\%$. Thus, the spin-imbalance degree of freedom will allow us to check to what extent the turbulent dynamics is sensitive to the vortex structure.

On this vortex lattice, we dynamically imprint either two or four dark solitons in planes approximately perpendicular to the vortices, but with slight tilts to break translation invariance, and imprint a π or $\pi/2$ phase shift between each domain (see the supplement [19] for details). Due to snaking instabilities, these solitons are not stable [41] and decay, producing new vortices that destabilize the lattice and lead to a vortex tangle.

In Fig. 2 we show selected snapshots from the TDASLDA simulation for spin-symmetric system ($P = 0\%$).

The calculation demonstrates the full life cycle of the vortex tangle, and is characterized by two generic stages: 1) the generation of the vortex tangle, and 2) its subsequent decay. During generation, energy from the imprinted solitons is transferred to hydrodynamic flow, increasing the total length L of the vortex lines. Once the maximum vortex length is reached, the decay process starts and energy in the vortices is transferred into various internal excitations, including phonons. This “decay” is mediated by vortex dynamics, reconnections, and

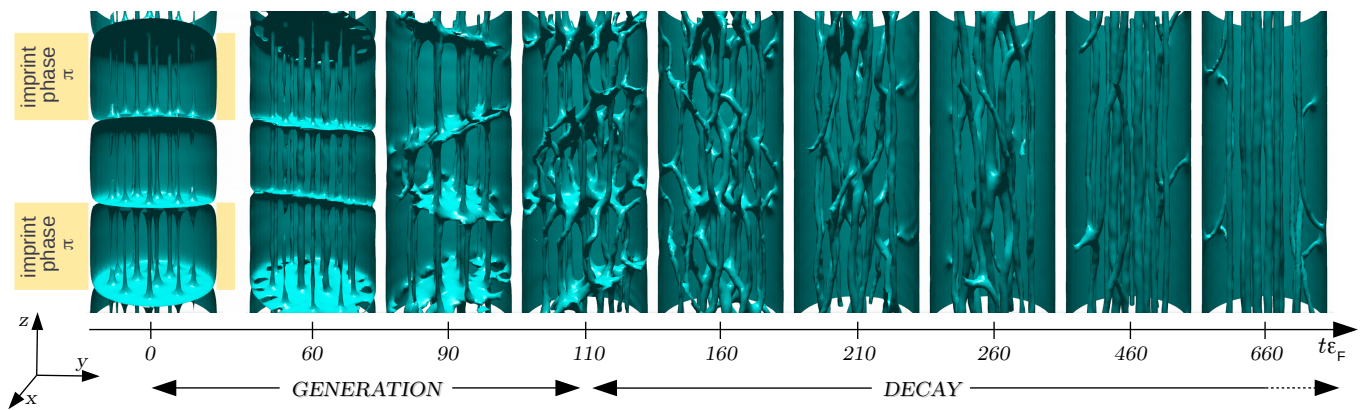


FIG. 2. Time evolution of the quantized vortex lines in the spin-balanced system $P = 0\%$ after imprinting four dark solitons with $\delta\varphi = \pi$ phase shifts across each. Figures display an isosurface for a constant value of the order parameter $\Delta(\mathbf{r})$ for selected moments in dimensionless time $t\varepsilon_F$. The moment of completion of the imprint procedure corresponds to initial time $t = 0$, and from this moment the system evolves freely where the total energy and the angular momentum L_z are conserved quantities. Below the time axis we indicate two time intervals where the total vortex line density increases (generation) and decreases (decay). For full movies see Supplemental Material [19].

crossings, allowing the system to relax back to a state consisting of the original vortex lattice embedded in an excited superfluid. After the phase imprinting procedure, the total energy E_{tot} , particle number N , and z component of the angular momentum L_z are being conserved. Numerically however, the discrete lattice breaks the axial symmetry: L_z is thus only approximately conserved to an accuracy of about 1% for the calculations presented here.

Rotating quantum turbulence in the TDASLDA — We analyze the total vortex line length $L(t)$ extracted from TDASLDA results for spin polarizations, $P = 0\% - 20\%$, starting with the initial states presented in Figs. 1(b)-(d), then imprinting the solitons, and evolving through the generation and decay stages. The results, normalized to the initial length $L(t)/L(0)$ are shown in Fig. 3. The vortex tangle takes about $\Delta t_{\text{gen.}} \approx 100\varepsilon_F^{-1}$ to generate, taking slightly longer time with increased polarization. We attribute this effect to the enhanced stability of dark solitons in spin-imbalanced Fermi systems [28, 42, 43].

The decay dynamics exhibit more interesting features, with two distinct regimes characterized by different rates of decay. We assume that the decay can be modelled by power law formula $L(t)/L(0) \sim t^{-\alpha}$, which empirically we find consistent with our data, however we emphasize that simulation volume does not allow for presence of many decades of length scales required for appearance of the postulated scaling law. The first decay regime lasts for about $\Delta t_{\text{decay}}^{(1)} \approx 100 - 150\varepsilon_F^{-1}$ after the establishment of maximum vortex line length at $t \approx 100\varepsilon_F^{-1}$. Here the decay follows the formula with $\alpha \approx 0.3$. This behavior seems to be insensitive to the spin imbalance of the system, suggesting that the dynamics in this regime is only weakly affected by the internal structure of vor-

tices, which depends strongly on the spin polarization $P \in (0\%, 20\%)$ as seen in Fig. 1. The second decay regime starts immediately after the first one and is governed by a different exponent, reduced by a factor of three, again being relatively insensitive to the spin imbalance. Since the system evolves towards a vortex lattice configuration, the value of $L(t)/L(0)$ will stabilize eventually at some constant value, which may differ from 1 corresponding to a different final number of vortices due to an exchange of angular momentum with the normal component: The quantum vortices measure only the angular momentum stored in superfluid component.

To clarify the origin of the two slope decay patterns, we track how many vortices touch the boundary of the tube $\#_b(t)$ and the spatial distribution of the reconnection events. In the first regime, the number of vortices attached to the boundary decreases, while in the second region, it stabilizes at a constant value. (See the histograms in Fig. 3.) The initial decay is accelerated by reconnections close to the boundary which expel vortex segments from the system, which occur on a variety of scales. A particularly large amplitude event occurs at $t\varepsilon_F \approx 250$ in the system with $P = 10\%$ spin polarization. This is shown in the insets **a.-c.** of Fig. 3, and is responsible for the localized increase in the decay rate circled in the main panel. Qualitatively similar results were obtained for simulations of turbulence in rotating ^3He [2], where vortex reconnections and annihilations were facilitated by the boundary. In the second (slower) regime of the decay, reconnection events are rare, taking place mainly in the bulk. These reconnections generate Kelvin waves that propagate along the vortex lines and dissipate into phonons. For both stages of the decay, the associated exponent is significantly different from the value

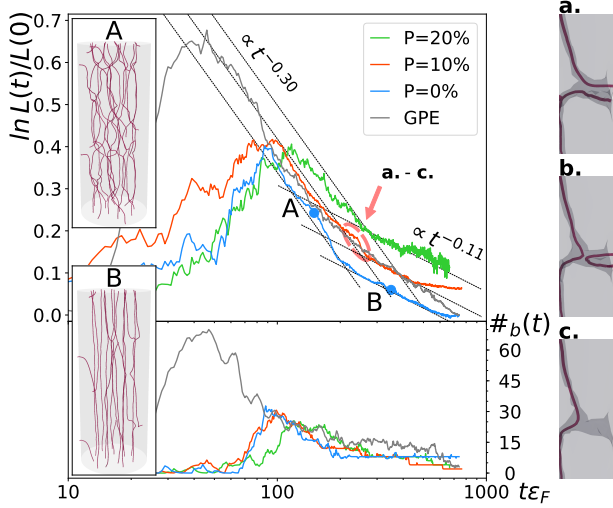


FIG. 3. Time evolution of the total vortex line length $L(t)$ normalized to the initial value $L(0)$ in log-log scale (lines on the main graph). Results of ASDA simulations are presented for different total polarizations $P = 0\%, 10\%, 20\%$ of the system and compared with GPE model (details in the text). The tangle of vortices is induced by imprinting four dark solitons on the preformed vortex lattices shown in Fig. 1. Black dashed lines demonstrate that the decay of the vortex tangle ($t\epsilon_F \gtrsim 100$) is consistent with a function of form $\sim t^{-\alpha}$ (see the text for a discussion). Typical configurations of the vortex tangle for two stages of the decay are visualized on insets **A** and **B**. The histograms show the number of vortex-line ends touching the boundary $\#_b(t)$ and we see a correlation between the decay rate and number of vortices touching the boundary. Insets **a.-c.** show the leading process responsible for the faster decay rate: vortex reconnection and annihilation near the boundary. Contours correspond to isosurfaces of $|\Delta(\mathbf{r})|$ and the red lines correspond to the vortex line found by the tracking algorithm. The insets **a.-c.** show fragments of a vortex tangle for the $P = 10\%$ case at the time marked with red dashed ellipse on the main plot.

predicted for Vinen turbulence: $L(t) \sim t^{-1}$. This is expected due to the effects related to the net rotation, and the presence of container walls [44].

To determine the universality of this turbulence (independence of the generation mechanism), we also induce a tangle with only two solitons. As shown in Fig. 4, the maximum total vortex length increases with the number of imprinted solitons

as is expected since the vortex tangle is induced by the solitons. In both cases, the maximum for $L(t)$ is attained approximately at the same time, followed by the same two regimes of decay with very similar decay slopes (dashed lines in Fig. 4).

Repeating the procedure with a phase difference of $\pi/2$ across the solitons produces a qualitative change. In this case, the solitons are “gray”, and move in the z -direction with a propagation velocity that depends on the phase difference $\delta\varphi$ that is maximal near unitar-

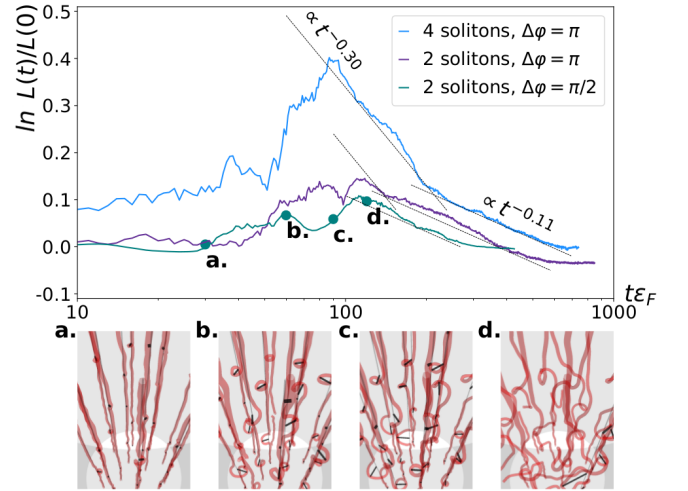


FIG. 4. Comparison of the total vortex line length $L(t)$ evolution with respect to the tangle generation methods. The total polarization of the system is $P = 0\%$. The number of solitons corresponds to the number of imprinted phase jumps of the order parameter $\Delta(\mathbf{r})$. Lines for the 2 soliton case are shifted down for better visibility. Imprinting a $\delta\varphi = \pi$ phase jump produces stationary dark solitons, while $\delta\varphi = \pi/2$ produces moving grey solitons. The latter leads to a Donnelly-Glaberson instability seen in insets **a.-d.** where the red lines indicate the tracked vortex line position, and the black segments show local maxima of Kelvin waves amplitude. We observe amplification of these amplitudes (**a.-c.**) leading to the vortex-vortex and vortex-boundary collisions (**d.**) that trigger the decay of $L(t)$. For full movies see the Supplemental Material [19].

ity $v_s \sim \cos \frac{\delta\varphi}{2}$ [45]. This induces a superfluid counterflow relative to the stationary normal component in the core of the vortices. When the counterflow exceeds critical value, the Donnelly-Glaberson (DG) instability occurs [46–48] which is seen as an increase in the amplitude of Kelvin waves induced on the vortices. These Kelvin waves are amplified until they reach the inter-vortex spacing, whereupon they interact with other vortices, creating a vortex tangle. (See panels (a)-(d) of Fig. 4.) Unlike the case with dark solitons (π phase difference), the second decay regime dominates. This is consistent with the generation of turbulence due to the DG instability, which creates a vortex tangle in the bulk, away from the boundaries. The DG instability was studied in atomic BECs as a tool for generating quantum turbulence [49], and we provide here the practical prescription for applying this mechanism in the UFG.

Comparison with the GPE —

We repeat the same procedure for spin-balanced systems $P = 0\%$ applying instead the GPE approach. The result is contrasted with TDASDA data in Fig. 3 where we see that the GPE can be tuned to give the same qualitative features as the TDASDA, including the initial

generation of turbulence, followed by decay regimes. To obtain such behavior, however, one has to tune the dissipation parameter η appropriately. It has been adjusted by comparing the dynamics with TDSLDA, and it was found that values $\eta \approx 0.01 - 0.02$ qualitatively preserve the two-stage nature of the decay. This provides a way to mock up the one and two-body losses built into the TDSLDA which convert hydrodynamic energy into internal energy but is absent in the pure GPE. In addition one has to correct for particle number and angular momentum L_z which otherwise are not conserved due to the presence of nonzero imaginary time component. To do this, we dynamically adjust the chemical potential μ to conserve particle number, and perform the simulation in a rotating frame with angular velocity Ω .

After the time evolution, we extract similar decay exponents as TDASLDA for the two-stages of the decay. Within the GPE framework, we find the exponents to be ≈ 0.33 and ≈ 0.11 , whereas TDASLDA produces ≈ 0.3 and ≈ 0.11 .

Conclusions— We have simulated dynamical quantum turbulence in a trapped rotating unitary Fermi gas with a microscopic density functional theory (TDASLDA), and identified two universal regimes of decay: one dominated by vortex reconnection near the boundary of the system, and the other dominated by vortex reconnection in the bulk. These qualitative effects can be reproduced by a computationally simpler orbital-free theory (GPE) by introducing an appropriately tuned dissipation while manually conserving particle number and angular momentum. Unlike the GPE, however, the TDASLDA requires no phenomenological parameters, hence is able to make predictions concerning the turbulent dynamics. In particular, the TDASLDA accounts for effects related to presence of a normal component, including the development of a Donnelly-Glaberson instability, which we show how to use to generate bulk turbulence. The TDASLDA allows also to study the effect of a spin imbalance, which significantly alter the structure of vortices, but surprisingly does not alter the turbulent dynamics qualitatively. The procedures used to generate turbulence are compatible with experimental capabilities, paving the way for experimenters to address some of the outstanding challenges in the field of quantum turbulence raised in [50]. In particular, we have demonstrated two different *mechanisms for generating turbulence* in an “*exotic*” system with *tunable interactions*: imprinting solitons which generates turbulence both in the bulk and near the boundaries, and through the Donnelly-Glaberson instability which primarily generates bulk turbulence. We also demonstrate the inclusion of *beyond mean-field* effects through an empirically established DFT that includes induced Hartree term which are absent in the traditional mean-field BdG approach. Interestingly, the TDASLDA develops quantum turbulence without the need for any additional dissipation, unlike the GPE, providing insight

into the microscopic *mechanism for vortex tangle generation* discussed in [50]. This provides a means for calibrating simpler GPE-like theories which may be crucial for understanding quantum turbulence in complex systems such as neutron stars.

ASLDA calculations were executed by G.W. and K.S. and GPE calculations were executed by K.H. and M.M.F. Data analysis was performed by K.K., G.W. and K.H. All authors contributed to discussion and interpretation of the results and to writing of the manuscript. This work was supported by the Polish National Science Center (NCN) under Contracts No. UMO-2017/26/E/ST3/00428 (GW) and UMO-2017/27/B/ST2/02792 (KK, PM), and the National Science Foundation through Grant No. PHY-1707691 (KH, MMF). We acknowledge PRACE for awarding us access to resource Piz Daint based in Switzerland at Swiss National Supercomputing Centre (CSCS), decision No. 2017174125. We also acknowledge the Global Scientific Information and Computing Center, Tokyo Institute of Technology for resources at TSUBAME3.0 (Project ID: hp180066 and hp190063) and the Interdisciplinary Centre for Mathematical and Computational Modelling (ICM) of Warsaw University for computing resources at Okeanos (grant No. GA76-13).

* gabriel.wlazlowski@pw.edu.pl

† konrad.kobuszewski.dokt@pw.edu.pl

‡ m.forbes@wsu.edu

- [1] A. A. Abrikosov, Nobel Lecture: Type-II superconductors and the vortex lattice, *Rev. Mod. Phys.* **76**, 975 (2004).
- [2] V. B. Eltsov, R. de Graaf, P. J. Heikkinen, J. J. Hosio, R. Hänninen, M. Krusius, and V. S. L’vov, Stability and Dissipation of Laminar Vortex Flow in Superfluid $^3\text{He-B}$, *Phys. Rev. Lett.* **105**, 125301 (2010).
- [3] V. Eltsov, R. Hänninen, and M. Krusius, Quantum turbulence in superfluids with wall-clamped normal component., *Proc. Natl. Acad. Sci. U. S. A.* **111** Suppl, 4711 (2014).
- [4] A. P. Finne, T. Araki, R. Blaauwgeers, V. B. Eltsov, N. B. Kopnin, M. Krusius, L. Skrbek, M. Tsubota, and G. E. Volovik, An intrinsic velocity-independent criterion for superfluid turbulence, *Nature* **424**, 1022 (2003).
- [5] J. J. Hosio, V. B. Eltsov, P. J. Heikkinen, R. Hänninen, M. Krusius, and V. S. L’vov, Energy and angular momentum balance in wall-bounded quantum turbulence at very low temperatures, *Nat. Commun.* **4**, 1614 (2013).
- [6] C. E. Swanson, C. F. Barenghi, and R. J. Donnelly, Rotation of a tangle of quantized vortex lines in He II, *Phys. Rev. Lett.* **50**, 190 (1983).
- [7] P. M. Walmsley and A. I. Golov, Rotating quantum turbulence in superfluid ^4He in the $T=0$ limit, *Phys. Rev. B* **86**, (2012).
- [8] S. Giorgini, L. P. Pitaevskii, and S. Stringari, Theory of ultracold atomic Fermi gases, *Rev. Mod. Phys.* **80**, 1215 (2008).

- [9] A. Bulgac, M. M. N. Forbes, and G. Wlazłowski, Towards quantum turbulence in cold atomic fermionic superfluids, *J. Phys. B* **50**, 014001, (2017).
- [10] C. F. Barenghi, R. J. Donnelly, and W. F. Vinen, *Quantized vortex dynamics and superfluid turbulence*, Lecture Notes in Physics, (Springer, 2001).
- [11] C. Pethick and H. Smith, *Bose-Einstein Condensation in Dilute Gases* (Cambridge University Press, 2002)
- [12] P. Pieri and G. C. Strinati, Derivation of the Gross-Pitaevskii Equation for Condensed Bosons from the Bogoliubov-de Gennes Equations for Superfluid Fermions, *Phys. Rev. Lett.* **91**, 030401 (2003).
- [13] Y. E. Kim and A. L. Zubarev, Time-dependent density-functional theory for trapped strongly interacting fermionic atoms, *Phys. Rev. A* **70**, 033612 (2004)
- [14] L. Salasnich and F. Toigo, Extended Thomas-Fermi density functional for the unitary Fermi gas, *Phys. Rev. A* **78**, 053626 (2008); Erratum: Extended Thomas-Fermi density functional for the unitary Fermi gas [*Phys. Rev. A* **78**, 053626 (2008)], *Phys. Rev. A* **82**, 059902(E) (2010)
- [15] L. Salasnich, Hydrodynamics of Bose and Fermi superfluids at zero temperature: the superfluid nonlinear Schrödinger equation, *Laser Phys.*, **19**, 642 (2009)
- [16] M.M. Forbes and R. Sharma, Validating Simple Dynamical Simulations of the Unitary Fermi Gas, *Phys. Rev. A* **90**, 043638 (2014).
- [17] S. Simonucci and G. C. Strinati, Equation for the superfluid gap obtained by coarse graining the Bogoliubov-de Gennes equations throughout the BCS-BEC crossover, *Phys. Rev. B* **89**, 054511 (2014).
- [18] S. Simonucci, P. Pieri, and G. C. Strinati, Vortex arrays in neutral trapped Fermi gases through the BCS-BEC crossover, *Nat. Phys.* **11**, 941 (2015).
- [19] See Supplemental Material at {URL will be provided by the publisher }, which includes Refs. [11, 20, 21], for explicit form of implemented equations, simulation parameters and list of supplemental movies.
- [20] M. Tsubota, K. Fujimoto, S. Yui, Numerical studies of quantum turbulence, *J. Low. Temp. Phys.* **188**, 119 (2017).
- [21] G. Krstulovic and M. Brachet, Comment on “Superfluid turbulence from quantum Kelvin wave to classical Kolmogorov cascades”, *Phys. Rev. Lett.* **105**, 129401 (2010).
- [22] A. Bulgac, P. Magierski, and M.M. Forbes, The Unitary Fermi Gas: From Monte Carlo to Density Functionals, in *BCS-BEC Crossover and the Unitary Fermi Gas*, edited by W. Zwerger, Lecture Notes in Physics (Springer, Heidelberg, 2012), Vol. **836**, pp 305-373.
- [23] A. Bulgac, and M.M. Forbes, Unitary Fermi Supersolid: The Larkin-Ovchinnikov Phase, *Phys. Rev. Lett.* **101**, 215301 (2008).
- [24] M. M. Forbes, S. Gandolfi, and A. Gezerlis, Resonantly interacting fermions in a box, *Phys. Rev. Lett.* **106**, 235303 (2011)
- [25] M. M. Forbes, S. Gandolfi, and A. Gezerlis, Effective-range dependence of resonantly interacting fermions, *Phys. Rev. A* **86**, 053603 (2012)
- [26] A. Bulgac, M.M. Forbes, M.M. Kelley, K.J. Roche, and G. Wlazłowski, Quantized Superfluid Vortex Rings in the Unitary Fermi Gas, *Phys. Rev. Lett.* **112**, 025301 (2014).
- [27] G. Wlazłowski, A. Bulgac, M.M. Forbes, and K.J. Roche, Life cycle of superfluid vortices and quantum turbulence in the unitary Fermi gas, *Phys. Rev. A* **91**, 031602(R) (2015).
- [28] G. Wlazłowski, K. Sekizawa, M. Marchwiany, and P. Magierski, Suppressed Solitonic Cascade in Spin-Imbalanced Superfluid Fermi Gas, *Phys. Rev. Lett.* **120**, 253002 (2018).
- [29] M. Machida and T. Koyama, Structure of a Quantized Vortex near the BCS-BEC Crossover in an Atomic Fermi Gas, *Phys. Rev. Lett.* **94**, 140401 (2005).
- [30] R. Sensarma, M. Randeria, and T.-L. Ho, Vortices in Superfluid Fermi Gases through the BEC to BCS Crossover, *Phys. Rev. Lett.* **96**, 090403 (2006).
- [31] A. Bulgac and Y. Yu, Vortex state in a strongly coupled dilute atomic fermionic superfluid, *Phys. Rev. Lett.* **91**, 190404 (2003).
- [32] M. Takahashi, T. Mizushima, M. Ichioka, and K. Machida, Vortex-core structure in neutral fermion superfluids with population imbalance, *Phys. Rev. Lett.* **97**, 180407 (2006).
- [33] H. Hu, X. J. Liu, and P. D. Drummond, Visualization of vortex bound states in polarized fermi gases at unitarity, *Phys. Rev. Lett.* **98**, 060406 (2007).
- [34] P. Magierski *et al.*, Spin-polarized vortex at the BCS-BEC crossover, in preparation.
- [35] A. Bulgac, Y.-L. Luo, P. Magierski, K.J. Roche, and Y. Yu, Real-time dynamics of aauntized vortices in a unitary Fermi superfluid, *Science* **332**, 1288 (2011).
- [36] I. Stetcu, C. Bertulani, A. Bulgac, P. Magierski, and K.J. Roche, Relativistic Coulomb excitation within Time Dependent Superfluid Local Density Approximation, *Phys. Rev. Lett.* **114**, 012701 (2015).
- [37] A. Bulgac, P. Magierski, K.J. Roche, and I. Stetcu, Induced Fission of ^{240}Pu within a Real-Time Microscopic Framework, *Phys. Rev. Lett.* **116**, 122504 (2016).
- [38] P. Magierski, K. Sekizawa, and G. Wlazłowski, Novel Role of Superfluidity in Low-Energy Nuclear Reactions, *Phys. Rev. Lett.* **119**, 042501 (2017).
- [39] G. Wlazłowski, K. Sekizawa, P. Magierski, A. Bulgac, and M.M. Forbes, Vortex Pinning and Dynamics in the Neutron Star Crust, *Phys. Rev. Lett.* **117**, 232701 (2016).
- [40] M.J.H. Ku, B. Mukherjee, T. Yefsah, and M.W. Zwierlein, Cascade of Solitonic Excitations in a Superfluid Fermi gas: From Planar Solitons to Vortex Rings and Lines, *Phys. Rev. Lett.* **116**, 045304 (2016).
- [41] A. Muñoz Mateo, X. Yu, and J. Nian, Vortex lines attached to dark solitons in Bose-Einstein condensates and boson-vortex duality in 3+1 dimensions, *Phys. Rev. A* **94**, 063623 (2016).
- [42] M.D. Reichl and E.J. Mueller, Core filling and snaking instability of dark solitons in spin-imbalanced superfluid Fermi gases, *Phys. Rev. A* **95**, 053637 (2017).
- [43] G. Lombardi, W. Van Alphen, S. N. Klimin, and J. Tempere, Snake instability of dark solitons across the BEC-BCS crossover: An effective-field-theory perspective, *Phys. Rev. A* **96**, 033609 (2017).
- [44] M. S. Mongiovì and D. Jou, Evolution equations in superfluid turbulence, in *Condensed Matter: New Research*, edited by M. P. Das, (Nova Science Pub Inc., New York, 2007), pp 1-53.
- [45] A. Spuntarelli, L. D. Carr, P. Pieri, and G. C. Strinati, Gray solitons in a strongly interacting superfluid Fermi gas, *New J. Phys.* **13**, 035010 (2011).
- [46] W. I. Glaberson, W. W. Johnson, and R. M. Ostermeier, Instability of a vortex array in He II, *Phys. Rev. Lett.* **33**, 1197 (1974).
- [47] R. M. Ostermeier and W. I. Glaberson, Instability of vor-

tex lines in the presence of axial normal fluid flow, J. Low Temp. Phys. **21**, 191 (1975).

- [48] M. Tsubota, T. Araki, and C. F. Barenghi, Rotating Superfluid Turbulence, Phys. Rev. Lett. **90**, 205301 (2003).
- [49] H. Takeuchi, K. Kasamatsu, and M. Tsubota, Spontaneous radiation and amplification of Kelvin waves on quantized vortices in Bose-Einstein condensates, Phys. Rev. A **79**, 033619 (2009).
- [50] L. Madeira, M. A. Caracanhas, F. E. A. dos Santos, and V. S. Bagnato, Quantum turbulence in quantum gases, Annu. Rev. Condens. Matter Phys. **11**, 37 (2020).
- [51] A. Villois, G. Krstulovic, D. Proment, and H. Salman, A vortex filament tracking method for the Gross-Pitaevskii model of a superfluid, J. Phys. A **49**, 415502 (2016).

SUPPLEMENTAL MATERIAL

In this Supplemental Material, we describe technical aspects related to: form of implemented equations, simulation details, extraction of vortex lines. We also provide a list of supplemental movies.

THEORETICAL FRAMEWORK

TDASLDA Equations

The calculations employ ASLDA functional described in details in paper [22]. The functional is defined via following spin-dependent ($i = \uparrow, \downarrow$) densities:

- particle number density:

$$n_i(\mathbf{r}) = \sum_{|E_n| < E_c} |v_{n,i}(\mathbf{r})|^2 f_\beta(-E_n) \quad (1)$$

- kinetic density:

$$\tau_i(\mathbf{r}) = \sum_{|E_n| < E_c} |\nabla v_{n,i}(\mathbf{r})|^2 f_\beta(-E_n), \quad (2)$$

- current density:

$$\mathbf{j}_i(\mathbf{r}) = \sum_{|E_n| < E_c} \text{Im}[v_{n,i}(\mathbf{r}) \nabla v_{n,i}^*(\mathbf{r})] f_\beta(-E_n), \quad (3)$$

- anomalous density:

$$\nu(\mathbf{r}) = \sum_{|E_n| < E_c} v_{n,\downarrow}^*(\mathbf{r}) u_{n,\uparrow}(\mathbf{r}) \frac{f_\beta(-E_n) - f_\beta(E_n)}{2}. \quad (4)$$

In the formulas we set units to $m = \hbar = k_B = 1$. The densities are parametrized in terms of Bogoliubov quasiparticle wave functions $\{v_{n,i}, u_{n,i}\}$. E_n is the quasiparticle energy and E_c is the energy cut-off as required by

the regularization scheme. The Fermi-Dirac distribution, $f_\beta(E) = 1/(\exp(\beta E) + 1)$ where $\beta = 1/T$, models finite-temperature effects. The structure of the ASLDA functional reads:

$$\mathcal{E}_{\text{ASLDA}} = \alpha_\uparrow(p) \frac{\tau_\uparrow}{2} + \alpha_\downarrow(p) \frac{\tau_\downarrow}{2} + \beta(p)(n_\uparrow + n_\downarrow)^{5/3} + \frac{\gamma(p)}{(n_\uparrow + n_\downarrow)^{1/3}} \nu^* \nu + \sum_{i=\uparrow, \downarrow} [1 - \alpha_i(p)] \frac{\mathbf{j}_i^2}{2n_i}. \quad (5)$$

The coupling constants α_i , β and γ are polynomial functions of the local polarization of the gas $p = \frac{n_\uparrow - n_\downarrow}{n_\uparrow + n_\downarrow}$. The polynomials coefficients have been adjusted to quantum Monte Carlo results for spin-imbalanced unitary Fermi gas, see [22] for details related to the fitting procedure.

The term in the functional that depends on the currents \mathbf{j}_i introduces significant cost to the computation. This term is responsible for maintaining Galilean invariance of the ASLDA theory. Since the effective mass was found to be consistent with the bare mass to within 10% for a large range of polarizations, in the calculations we set $\alpha_i = 1$. Therefore, the particular form of the functional used in this paper simplifies to:

$$\mathcal{E}_{\alpha=1} = \frac{1}{2}(\tau_\uparrow + \tau_\downarrow) + \beta(p)(n_\uparrow + n_\downarrow)^{5/3} + \frac{\gamma}{(n_\uparrow + n_\downarrow)^{1/3}} \nu^* \nu. \quad (6)$$

The TDASLDA equations are obtained from the stationarity condition of the action,

$$S = \int_{t_0}^{t_1} \left(\langle 0(t) | i \frac{d}{dt} | 0(t) \rangle - E(t) \right) dt, \quad (7)$$

with respect to variation of Bogoliubov quasi-particle wave functions, where $|0(t)\rangle$ denotes the quasiparticle vacuum at time t and $E(t)$ is the total energy

$$E(t) = \int \left(\mathcal{E}_{\alpha=1}(\mathbf{r}, t) + \sum_{i=\uparrow, \downarrow} V_i(\mathbf{r}, t) n_i(\mathbf{r}, t) \right) d\mathbf{r}. \quad (8)$$

V_i is the external potential, described later. Resulting equations of motion are the following:

$$i \frac{\partial}{\partial t} \begin{pmatrix} u_{n,\uparrow}(\mathbf{r}, t) \\ v_{n,\downarrow}(\mathbf{r}, t) \end{pmatrix} = \begin{pmatrix} h_\uparrow(\mathbf{r}, t) & \Delta(\mathbf{r}, t) \\ \Delta^*(\mathbf{r}, t) & -h_\downarrow^*(\mathbf{r}, t) \end{pmatrix} \begin{pmatrix} u_{n,\uparrow}(\mathbf{r}, t) \\ v_{n,\downarrow}(\mathbf{r}, t) \end{pmatrix} \quad (9)$$

where the single-particle hamiltonian and pairing potentials take, respectively, the following forms:

$$h_i(\mathbf{r}, t) = -\frac{1}{2} \nabla^2 + \frac{\delta \mathcal{E}_{\alpha=1}}{\delta n_i}(\mathbf{r}, t) \delta n_i + V_i(\mathbf{r}, t) - \mu_i, \quad (10)$$

$$\Delta(\mathbf{r}, t) = -\frac{\delta \mathcal{E}_{\alpha=1}}{\delta \nu^*}(\mathbf{r}, t). \quad (11)$$

Note, that the pairing coupling constant γ entering the equation for $\Delta(\mathbf{r}, t)$ is subject of regularization procedure

as described in [22]. Chemical potentials μ_i are meaningful only in case of static variant of Eq. (9), i.e. $i\frac{\partial}{\partial t} \rightarrow E_n$, and are adjusted in such a way to obtain requested particle number N_i . The spin reversed components of quasiparticle wavefunctions are obtained via the symmetry relation $u_{n,\uparrow} \rightarrow v_{n,\uparrow}^*$, $v_{n,\downarrow} \rightarrow u_{n,\downarrow}^*$ and $E_n \rightarrow -E_n$.

For time integration we used 5th order Adams-Bashforth-Moulton (predictor-corrector) scheme. The integration time step Δt was taken to be $\Delta t E_{\max} = 0.035$, where $E_{\max} = \pi^2/2dx^2$ is estimation of the maximum energy that can be resolved on employed spatial lattice with spacing dx .

GPE model

We compare these results to an GPE simulation of the form described in [16] for the dimer/Cooper-pair wavefunction $\Psi(\mathbf{r}, t)$ with mass $m_D = 2m$ and dimer number-density $n_D = n_F/2 = |\Psi|^2$, replacing the GPE energy-density $gn_D^2/2$ by the energy-density of the UFG $\xi\mathcal{E}_{FG}(n_F)$.

$$ie^{i\eta}\dot{\Psi} = \left(-\frac{1}{4m}\nabla^2 + 2\xi\mathcal{E}'_{FG}(n_F) + 2V - \mu + \Omega\hat{L}_z \right) \Psi \quad (12)$$

with $\mathcal{E}'_{FG} = \frac{3}{5}\varepsilon_F n_F$, $\varepsilon_F = \frac{\hbar^2 k_F^2}{2m_F}$, $\xi = 0.373$.

Here, E_{FG} is the energy of the free Fermi gas. The GPE lacks any mechanism for dissipating hydrodynamic energy into internal degrees of freedom (i.e. one-body dissipation). To account for this, we introduce a small amount of dissipation by hand through the phase $\eta \sim 0.01$. To ensure conservation of particle number and approximate conservation of angular momentum, we include a dynamically adjusted chemical potential $\mu[\Psi]$ and simulate in a co-rotating frame with angular velocity Ω matching the initial state. With these modifications, the GPE model (12) provides a qualitatively similar description of the turbulent phenomena we see in the TDASLDA.

SIMULATION DETAILS

TDASLDA simulations details

Generation of the initial state The initial state for the simulations is obtained as a solution of static ASLDA equations, which are obtained from Eq. (9) by requiring stationarity of solutions: $v_i(\mathbf{r}, t) = \exp(-iEt)v_i(\mathbf{r})$, $u_i(\mathbf{r}, t) = \exp(-iEt)u_i(\mathbf{r})$. The external potential has

the form (distances are expressed in lattice units dx):

$$V_{\text{trap}}(x, y) = \begin{cases} 0, & \rho \leq 17.5 \\ 5\varepsilon_F s(\rho - 17.5, 7.5), & 17.5 < \rho < 25 \\ 5\varepsilon_F, & \rho \geq 25 \end{cases} \quad (13)$$

where $\rho = \sqrt{x^2 + y^2}$ is the distance from the symmetry z -axis and s denotes the switching function

$$s(x, w) = \frac{1}{2} + \frac{1}{2} \tanh \left[\tan \left(\frac{\pi x}{w} - \frac{\pi}{2} \right) \right], \quad (14)$$

which smoothly rises from 0 to 1 over distance w . Since the trapping potential does not depend on z the quasiparticle wave functions acquire generic form $\varphi(\mathbf{r}) \rightarrow \varphi(x, y)e^{ik_z z}$ and 3D static problem effectively reduces to 2D problem which needs to be solved for each quantum number k_z .

In order to start with solution containing the vortex lattice the ASLDA equations were solved in rotating frame. It accounts for adding to the single particle hamiltonian (10):

$$h_i(\mathbf{r}) \rightarrow h_i(\mathbf{r}) - \Omega L_z, \quad (15)$$

where $L_z = -ix\frac{\partial}{\partial y} + iy\frac{\partial}{\partial x}$ is z -th component of the angular momentum operator. The ASLDA equations were solved self-consistently.

Dynamical generation of the turbulent state The turbulent state is generated dynamically by applying time-dependent external potential:

$$V(\mathbf{r}, t) = V_{\text{trap}}(x, y) + V_{\text{knives}}(\mathbf{r}, t) + V_{\text{impr.}}(\mathbf{r}, t). \quad (16)$$

Potential V_{knives} is used to separate the gas into segments, see first panel of Fig. 2 (main article). It has form:

$$V_{\text{knives}}(\mathbf{r}, t) = \sum_{k=1}^K A(t) \exp \left(-\frac{(z - z_k(x, y))^2}{2\sigma^2} \right), \quad (17)$$

where K denotes the number of knives (we did simulations for $K = 2$ and 4) and z_k is position of a given knife potential:

$$z_k(x, y) = k \frac{N_z}{K} + r_1 x + r_2 y, \quad (18)$$

where r_1 and r_2 are randomly selected small numbers ($r \ll 1$). Thus, the knives are evenly distributed along z axis with spacing $\frac{N_z}{K}$ and each of them is independently tilted with respect to xy plane. The random tilts break periodic symmetry along z direction. The width of the knife potential was taken $\sigma \approx 2dx$. The time-dependent amplitude of knives potential was changing in the following way (see Fig. 5):

1. we start simulations with $A = 0$ and gradually raise it up to value $A_{\max} = 2.5\varepsilon_F$ in the time interval $\Delta t_{\text{rise}} \approx 150\varepsilon_F^{-1}$,

2. next, we keep the amplitude at fixed value for time interval $\approx 100\varepsilon_F^{-1}$
3. finally, in short time interval $\Delta t_{\text{off}} \approx 10\varepsilon_F^{-1}$ we turn-off the knives.

The time when we start to turn-off knife potentials is indicated as $t = 0$.

The phase imprint is realized by turning on for some time interval $\Delta t_{\text{impr.}}$ the external potential $V_{\text{impr.}}$. It is a constant potential that is applied only to selected segments of the cloud, indicated by yellow boxes on Fig. 2 (main article). The pairing field is proportional to the anomalous density $\nu \sim \sum_n v_{n,\downarrow}^* u_{n,\uparrow}$ and it evolves as $\Delta = e^{2i\mu t}|\Delta|$ where μ is the chemical potential. For segments that are subject of the phase imprinting potential we have $\Delta = e^{2i(\mu - U_0)t}|\Delta|$, where U_0 is strength of the potential. Consequently after time $\Delta t_{\text{impr.}}$ the phase for imprinted segments gets an extra shift $\delta\varphi = 2U_0\Delta t_{\text{impr.}}$. The strength of the potential U_0 is adjusted to introduce the requested phase difference $\delta\varphi$ within a time interval $\Delta t_{\text{impr.}}\varepsilon_F \approx 75$.

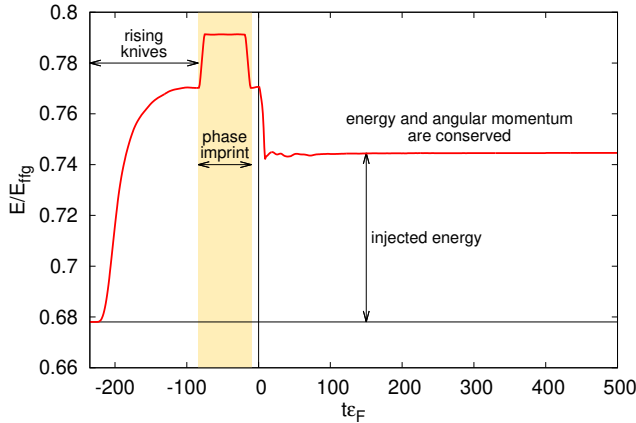


FIG. 5. Time evolution of the total energy (expressed in units of free Fermi gas energy $E_{\text{ffg}} = \frac{3}{5}N\varepsilon_F$) in simulations for $P = 0\%$ where turbulence is generated by introducing 4 knives and imprinting phase difference is π .

In Fig. 5 we show a representative graph showing the total energy changes for different stages of the state preparation ($t < 0$) and subsequently for evolution ($t > 0$) which is subject of observation. The stages related to applying knives, phase imprinting and removing knives are clearly visible. The difference between energy of the initial (derived from static calculations) state and energy which is subject of the observation measures amount of energy which was injected to the system. We also checked that main properties of the tangle evolution do not depend on values of $\Delta t_{\text{impr.}}$ and Δt_{rise} .

GPE simulations

To generate the initial state for the GPE simulations, we set our lattice spacing as described in the main text and the chemical potential $\mu = 0.5\xi\varepsilon_F$ in the same external potential in Eq. (13). The trap hosts ≈ 3700 particles. Then we imprint 14 vortices and minimize the state with fixed number of particles in a rotating frame with $\Omega = -0.05\varepsilon_F$ to get a solution of the GPE similar to that of ASLDA with $P=0\%$ in 2D. This solution is then used to populate the 3D state with periodic boundary condition in z-direction. Then we evolve the 3D state using Eq. (12) to dynamically generate turbulence following the same procedure described in the “Dynamical generation of the turbulent state” section. Then we evolve the turbulent state with different dissipation parameters to study the life cycle of the state.

The initial state that we generate in this process is similar to ASLDA initial state, with a couple of minute differences in the arrangement of the vortices and number of particles. These differences does not modify the qualitative physics greatly. In Fig. 6 we present results dependence on particular choice of the dissipation coefficient. It is visible, that the change of amount of the dissipation does not impact result at qualitative level, only quantitative changes as observed.

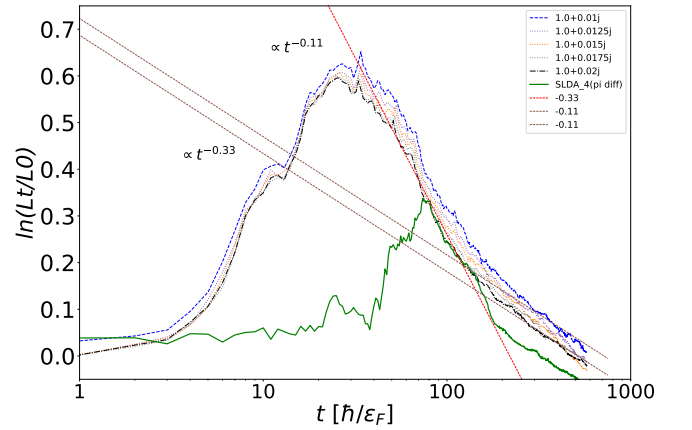


FIG. 6. Time evolution of the total vortex line length $L(t)$ normalized to the initial value $L(0)$ in log-log scale within GPE framework with different dissipation parameters. Comparison with the ASLDA simulations are presented for different total polarization $P = 0\%$. In the representative case shown in this figure the tangle of vortices is induced by imprinting four dark solitons with π phase shift across each of them, on the preformed vortex lattices shown in the figure 1 of the main text. We have explored $\eta = 0.01$ (dashed line) to $\eta = 0.02$ (dashed-dotted line) with 0.025 (dotted lines in between) interval. Dashed straight lines are guiding lines to show the trend and the two-stage nature of the decay.

INVESTIGATION OF VORTEX TANGLE PROPERTIES

Vortex detection algorithm

The vortex detection algorithm is based on the modification of the procedure presented in Ref. [51]. The algorithm consists of the following steps:

1. For a given spatial point \mathbf{r}_g (initial guess) we evaluate pseudovorticity $\boldsymbol{\omega}_{ps}(\mathbf{r}_g) = \nabla \times \mathbf{j}(\mathbf{r})|_{\mathbf{r}=\mathbf{r}_g}$ and create plane M that is normal (perpendicular) to the evaluated $\boldsymbol{\omega}_{ps}(\mathbf{r}_g)$ vector. It is assumed that the guess point is located close to the vortex core.
2. Within the plane M we search for point around which the phase of the order parameter Δ rotates by 2π . The phase is sampled for $k = 8$ points uniformly distributed on a circle with radius R constructed around point \mathbf{r}_g . Initial value of the circle radius is $0.75dx$. Next, the vortex core is searched by repeatedly applying operations:
 - (a) the radius of the circle is decreasing with step $dR = 0.05dx$ until the phase pattern along the circle loses monotonicity property, see panel (a) of Fig. 7;
 - (b) position of the circle is shifting $\mathbf{r}_g + d\mathbf{r} \rightarrow \mathbf{r}_g$ in such a way to restore the expected phase pattern, see panel (b) of Fig. 7.

The points (a)-(b) are executed until the radius reaches value $R = 0.05dx$ which sets accuracy of the vortex location detection. The center of the circle is assigned to the vortex position \mathbf{r}_v .

3. For the vortex core position \mathbf{r}_v the pseudovorticity is recalculated $\boldsymbol{\omega}_{ps}(\mathbf{r}_v) = \nabla \times \mathbf{j}(\mathbf{r})|_{\mathbf{r}=\mathbf{r}_v}$ and new guess point is created: $\mathbf{r}_g = \mathbf{r}_v + \frac{dx}{3} \frac{\boldsymbol{\omega}_{ps}(\mathbf{r}_v)}{|\boldsymbol{\omega}_{ps}(\mathbf{r}_v)|}$.

The points 1–3 are executed till the reconstructed vortex line either touches boundaries or creates closed loop. The first guess point for each line is located by analyzing the phase pattern for lattice plates.

The procedure described above was used to obtain vortex lines' positions for TDALSDA and TDGPE simulations after every $\delta t \varepsilon_F = 1$. Such time resolution guarantees that in co-rotating frame the ending of each vortex line lies sufficiently close (we assumed distance of $1.5dx$) to the same vortex line ending in the previous time step, which allows for temporal tracking of vortices. We use abrupt changes of vortex ends positions between two consecutive time frames as indicator of reconnection, annihilation or tearing of vortices.

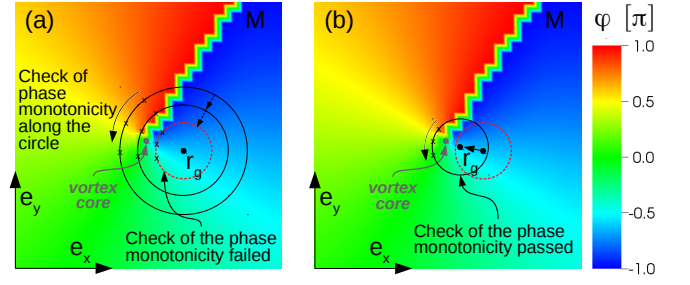


FIG. 7. Visualization of main part of the vortex detection algorithm: steps 2.(a) and 2.(b), see text for more details. Color map encodes the phase pattern of the order parameter $\varphi = \arg(\Delta)$.

Quantities characterizing vortex tangle

- Total length of vortices $L(t)$ – calculated as a sum of distances between consecutive points lying on distinct vortex lines (the points are given by the detection algorithm).
- Number of ends of vortices touching the boundary $\#_b(t)$ – extracted as vortex ends lying sufficiently close ($2dx$) to isosurface of low density region.
- Number of vortices $N_V(t)$ – the vortex lines can be distinguished basing on the mutual distance between pairs of the points given by the detection algorithm (the periodic boundary condition along z-axis is also taken into account).

LIST OF MOVIES

Below we provide the list of accompanying movies. All movies are also accessible on YouTube. There are two types of visualization:

vis1: Visualization of contour plot of $|\Delta|$. Left upper panel shows corresponding total length of vortex lines, while left bottom panel shows integrated along z direction value of $|\Delta|^2$, i.e. $\rho_{2d}(x, y) = \int |\Delta(x, y, z)|^2 dz$.

vis2: Visualization of vortex tangle. Central panel shows vortex lines given as output of vortex detection algorithm and isocontours of $|\Delta|$, left upper panel shows corresponding total length of vortex lines, left bottom panel shows occurrence of reconnection events (current ones are marked with red color) and right upper and bottom panels are number of vortex ends touching boundary $\#_b$ and number of vortices N_V , respectively.

List of movies with description:

Movies 1 and 7:: TDASLDA and GPE simulation demonstrating development and decay of rotating turbulence in the spin-symmetric UFG. The turbulence was generated by imprinting 4 solitons with a phase difference of π . Frames from this movie were used for Fig. 2 of main paper.

TDSLDA:

Files: Movie1-vis1, Movie1-vis2

YouTube: <https://youtu.be/5NiFRymHPYk>,
<https://youtu.be/yAtXReicxBY>;

GPE (in a co-rotating frame):

Files: Movie7-vis1, Movie7-vis2

YouTube: <https://youtu.be/EFwJ2v0tmzQ>,
<https://youtu.be/tPS1WIF7rUU>

Movie 2:: TDASLDA simulation demonstrating development and decay of rotating turbulence in the spin-imbalanced UFG with total polarization $P = 10\%$. All other conditions are the same as for *Movie 1*.

Files: Movie2-vis1, Movie2-vis2

YouTube: <https://youtu.be/imnsogKVhHQ>,
<https://youtu.be/ng44ojYDuHw>

Movie 3:: The same as *Movie 2*, but for total polarization $P = 20\%$

Files: Movie3-vis1, Movie3-vis2

YouTube: <https://youtu.be/h82ApFUwkI8>,
<https://youtu.be/6eEPsNJrJ58>

Movies 4 and 8:: TDASLDA and GPE simulations where turbulence was generated by imprinting 2

solitons with phase difference of π . Qualitatively the movie is similar to *Movies 1*.

TDSLDA:

Files: Movie4-vis1, Movie4-vis2

YouTube: https://youtu.be/zNilo_bSrCk,
<https://youtu.be/v72nPV7OMxQ>;

GPE (in a co-rotating frame):

Files: Movie8-vis1, Movie8-vis2

YouTube: <https://youtu.be/rrNRMMkqTj4>,
<https://youtu.be/SeYT8Evynjo>

Movies 5 and 9:: The same as *Movies 4 and 8*, except value of the imprinted of phase difference which here is $\pi/2$. This imprint generates moving solitons which induce amplification of kelvin waves.

TDSLDA:

Files: Movie5-vis1, Movie5-vis2

YouTube: <https://youtu.be/U8r5yiz3PPY>,
<https://youtu.be/EAzKumyddI>;

GPE (in a co-rotating frame):

Files: Movie9-vis1, Movie9-vis2

YouTube: <https://youtu.be/-FSJkcwZGOM>,
<https://youtu.be/gREn5kB3q0E>

Movie 6:: Movie showing result of collision of clouds with vortices where the phase imprint procedure is not applied. In such case the vortex tangle is not generated.

Files: Movie6-vis1, Movie6-vis2

YouTube: <https://youtu.be/HYSou4qK8fQ>,
<https://youtu.be/S3WTbvIFqY4>